ATLAS NOTE

ATL-INDET-PUB-2014-001

March 18, 2014
Revision: May 19, 2014

Basic ATLAS TRT performance studies of Run 1

The ATLAS Collaboration

Abstract

This document compares the results of basic performance studies of the ATLAS Transition Radiation Tracker (TRT) for data recorded during the 2011 and 2012 LHC running to the corresponding detector simulation studies. Electrons and muons from Z and J/ψ decays are used to characterize important performance aspects of the TRT as straw efficiency, drift-time accuracy, tracking and particle identification performance.

The following important corrections have been applied in this version, together with improvements to some of the text: Figures 14-18 were sourced incorrectly, the new figures show slightly improved agreement between simulation and data. Figures 19-26 are corrected for small typographical mistakes. The caption of Figures 53 and 54 incorrectly referred to μ values instead of occupancy values.

ATL-INDET-PUB-2014-001
19/05/2014

1 Introduction

This document compares the experimentally measured performance of the ATLAS transition radiation tracker (TRT) for data recorded in 2011 and 2012 to the corresponding detector simulation studies.

The Inner Detector (ID) of the ATLAS experiment [1] is designed to provide pattern recognition, electron identification, track momentum and both primary and secondary vertex measurement capabilities within the pseudorapidity range $|\eta|$ <2.5.

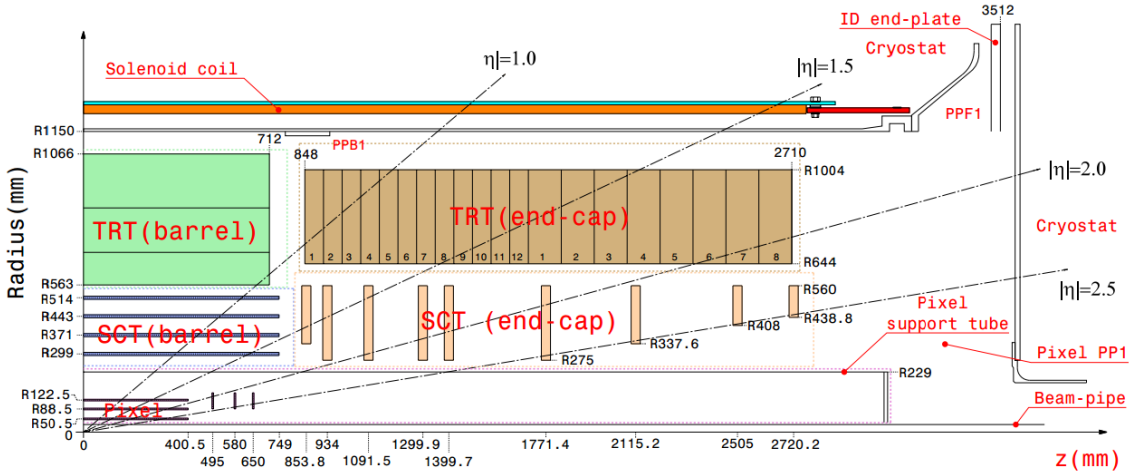

Figure 1: The Inner Detector (ID) of the ATLAS experiment viewed in *r*-*z*. Only the positive z side is shown.

The ID, shown in Figure 1, is contained within a cylindrical region of ±3.5 m and a radius of 1.15 m, in a solenoidal magnetic field of 2 Tesla. It consists of three sub-detectors. At inner radii, high resolution pattern recognition capabilities are available using discrete space points from silicon pixel and microstrip (SCT) layers. At larger radii, the transition radiation tracker (TRT) [2, 3, 4] consists of many layers of thin-walled proportional drift tubes, the so-called straw tubes, interleaved with radiator material to produce transition radiation. The TRT covers the pseudorapidity region $|\eta|$ <2.0 and has continuous tracking to enhance the pattern recognition, to improve the momentum resolution, and to provide electron identification using the signal from transition radiation (TR) photons. The low energy (5-25 keV) TR photons are absorbed in the Xe-based gas mixture of the drift tubes, and yield much larger signal amplitudes than minimum ionizing particles.

Tracking information and TR signals are obtained for each individual straw using separate low and high threshold discriminators in the front-end electronics. The low level threshold (typically 270 eV) is used for track position measurement in the straw and the high level threshold ($\approx$ 6 keV) is used to separate minimum ionizing particles from particles with high ionization or large Lorentz γ-factor (above ~2000) due to transition radiation absorbed in the active gas.

The barrel TRT is divided into 3 layers of modules in the radial direction and 32 sectors in ϕ. The straw tubes of the barrel TRT are 144 cm long and are oriented along the beam line. To reduce occupancy, the signal wires are electrically split at the center of each tube and read out from both ends. In the inner modules (Layer 0), wires of the first 9 straw layers are divided into 3 segments keeping only the outer 31.2 cm wire segments active from both sides. The space between straws is filled with the TR radiators which consist of polypropylene fibres of 15 μm diameter.

The TRT end-caps each consist of 2 types of independent wheels (type A and B) with straws oriented radially. The type A wheels are closer to the interaction point and consist of 12 wheels, each with 8 successive layers spaced 8 mm apart. The type B wheels are further from the interaction point starting

after the last type A wheel and consist of 8 wheels, also with 8 straw layers but spaced 15 mm apart. Each end-cap therefore has a total of 160 straw layers along the z-axis. Each layer contains 768 radially oriented straws of 37 cm length with uniform azimuthal spacing. Successive straw layers are staggered in ϕ to ensure full coverage of all tracks at all radii within the wheels. The space between successive straw layers is filled with layers of 15 mm thick polypropylene radiator foils separated by a polypropylene net.

For high p_{T} tracks originating from the interaction point, the design of the TRT ensures a large number of crossed straws (typically above 30) in the pseudorapidity range of $|\eta|$ <2.0. Some results presented here use pseudorapidity to separate regions of the detector as follows: $|\eta| < 0.625$ (tracks entirely in the TRT barrel), $0.625 < |\eta| < 1.070$ (tracks spanning the service region between the barrel and end-cap), $1.070 < |\eta| < 1.304$ (tracks in the type A end-cap wheels), $1.304 < |\eta| < 1.752$ (tracks spanning the type A and B end-cap wheels), $1.752 < |\eta| < 2.0$ (tracks entirely in the type B wheel region).

The detector response is simulated with the ATLAS simulation framework [5] using GEANT4 [6]. Recent developments improving the performance of the simulation include modeling of the attenuation of signal in the straw anode wires, and the introduction of additional η dependence of TR yield in the barrel region. The latter correction reflects a real dependence of the TR yield for the barrel radiator which depends on the incident angle of the particle to fibre radiator sheets from which the barrel part of the TRT was built. Because the exact threshold used during operation was known with some uncertainty, low level and high level threshold tuning has been performed in the simulation. The low threshold was tuned to match straw efficiency, and the high threshold was tuned to obtain agreement for the probability for a hit from minimum ionizing particles to pass the high threshold.

To provide pure samples, electrons and muons from J/ψ and Z decays were used in both data and simulation. The simulation is reweighted using the standard ATLAS algorithm to obtain the same distribution of pile-up as observed in the data.

Plots relating to different performance parameters are presented in sections as described below. Section 2 presents the comparison of simulation with data for the straw efficiency. The results of drift-time accuracy studies are presented in Section 3. The dependence on the average number of interactions per bunch crossing ($\langle\mu\rangle$) is also shown for both simulation and data. Leading-edge time distributions at different pile-up conditions are compared for simulation and data.

In Section 4 probabilities to exceed high level threshold for muons of different energies are presented. These plots mainly demonstrate the performance of GEANT4 and Photon Absorption Ionization (PAI) dE/dx model simulation. Detailed comparisons are made for electrons in Section 5 which produce not only dE/dx but also transition radiation. Section 6 presents simulation and data comparison for the probability to exceed high level threshold as a function of particle Lorentz γ-factor. In these high threshold probability studies, only data from 2011 is used because of electronics gain degradation due to radiation damage in 2012. The results presented here can be considered as stable for low occupancy. Radiation damage effects of the TRT FE chips were not corrected in 2012 but in the future a dedicated calibration procedure will be introduced to compensate for such kind of effects.

Results of the tracking studies for high pile-up (up to $\langle\mu\rangle = 70$) are presented in Sections 7 and 8. Section 7 compares data and simulation for TRT occupancy as a function of $\langle\mu\rangle$. Results of tracking studies inside of jets at high pile-up conditions are presented in Section 8.

2 Straw efficiency

Figures 2-7 show the TRT straw efficiency for muons from Z decays selected from 2011 and 2012 runs with 50 ns bunch crossings. The straw efficiency is the probability to give a signal above low level threshold from a particle crossing the straw at a certain distance from the anode wire. This diminishes significantly in the regions where the track passes close to the edge of the straw due to the shorter ionization path length.

The straw efficiency is sensitive to the low threshold discrimination setting. This setting in the simulation is tuned, at low $\langle\mu\rangle$, to obtain agreement with data for the plateau region of the distributions of straw efficiency versus track-to-wire distance (the distance of closest approach of the fitted track to the anode wire), separately for the barrel and end-cap regions. The results show that at significantly higher values of $\langle\mu\rangle$ (up to 30) the straw efficiency remains in good agreement.

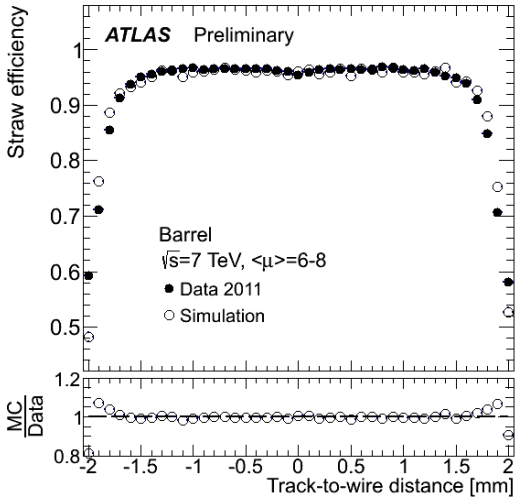

Figure 2: Straw efficiency in the TRT barrel versus track-to-wire-distance for decay muons from the channel $Z \rightarrow \mu^+\mu^-$. Data (solid circles) and simulation (open circles) are shown for $6 < \langle\mu\rangle < 8$ during 2011 at $\sqrt{s} = 7$ TeV.

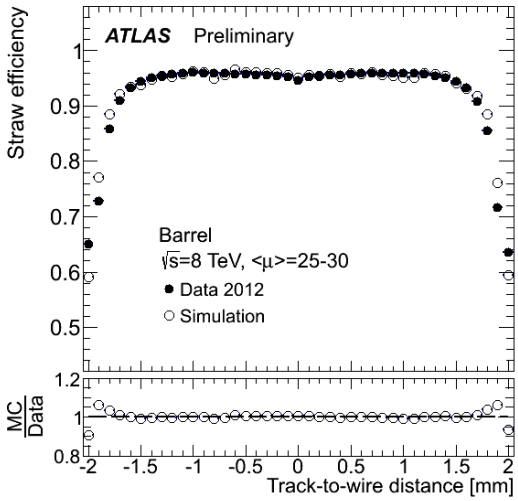

Figure 3: Straw efficiency in the TRT barrel versus track-to-wire-distance for decay muons from the channel $Z \rightarrow \mu^+\mu^-$. Data (solid circles) and simulation (open circles) are shown for $25 < \langle\mu\rangle < 30$ during 2012 at $\sqrt{s} = 8$ TeV.

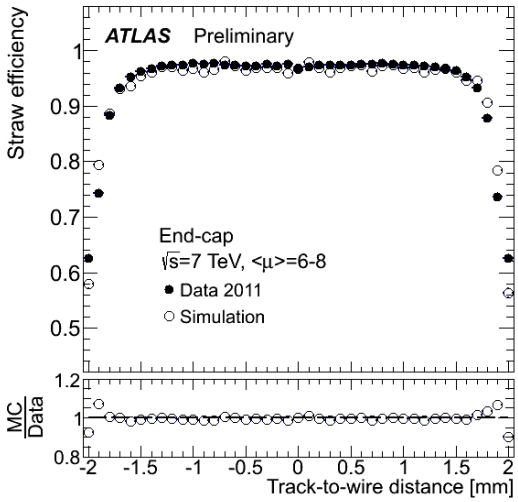

Figure 4: Straw efficiency in the TRT end-cap versus track-to-wire-distance for decay muons from the channel $Z \rightarrow \mu^+\mu^-$. Data (solid circles) and simulation (open circles) are shown for $6 < \langle\mu\rangle < 8$ during 2011 at $\sqrt{s} = 7$ TeV.

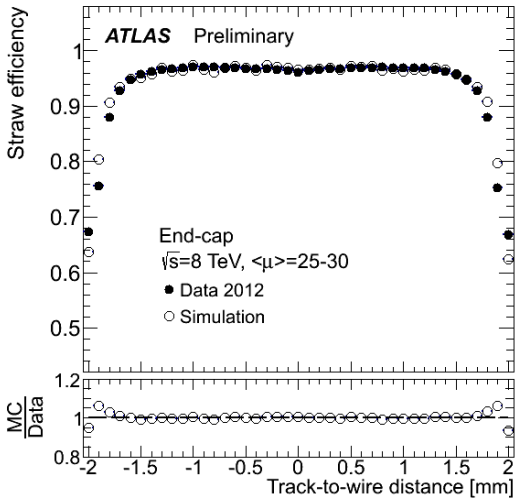

Figure 5: Straw efficiency in the TRT end-cap versus track-to-wire-distance for decay muons from the channel $Z \rightarrow \mu^+\mu^-$. Data (solid circles) and simulation (open circles) are shown for $25 < \langle\mu\rangle < 30$ during 2012 at $\sqrt{s} = 8$ TeV.

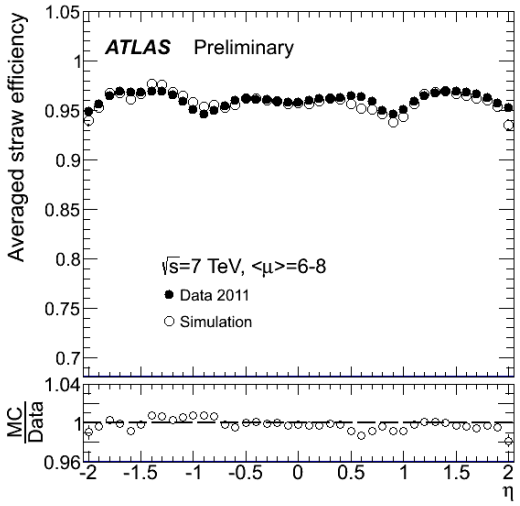

Figure 6: Average straw efficiency versus η for decay muons from the channel $Z \rightarrow \mu^+\mu^-$. Data (solid circles) and simulation (open circles) are shown for $6 < \langle\mu\rangle < 8$ during 2011 at $\sqrt{s} = 7$ TeV.

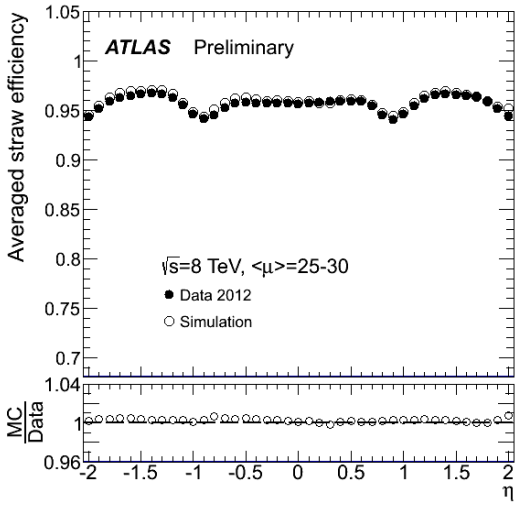

Figure 7: Average straw efficiency versus η for decay muons from the channel $Z \rightarrow \mu^+\mu^-$. Data (solid circles) and simulation (open circles) are shown for $25 < \langle\mu\rangle < 30$ during 2012 at $\sqrt{s} = 8$ TeV.

3 Drift-time accuracy studies

This section presents TRT performance plots based on drift-time measurements. Leading-edge time distributions and track position measurement accuracy are discussed.

The TRT measures the spatial position of tracks using drift-time measurements provided by recording the time at which the ionization signal exceeds the low level threshold (leading-edge time). A calibration procedure [7] calculates the relationship between the measured drift-time and the distance between the closest approach of the track to the anode wire, known as the *r-t* relationship. Using this *r-t* relation each leading-edge time measurement is translated into a measured drift-radius.

A precise simulation of the drift-time measurement relies on a detailed model of the drift-tube including: ionization of the gas, electron drift, energy fluctuations, signal propagation in the wire, signal shaping and discrimination.

The results obtained in this section are derived using muons taken between May and June of the 2012 pp running where the average number of interactions per bunch crossing was in the range $5 \leq \langle\mu\rangle \leq 30$. Muons from Z boson decays were selected requiring an angular separation of $\Delta R > 0.3$ between candidates and $p_{\mathrm{T}} > 15$ GeV. The reconstructed di-muon mass was required to be within $75 < M_{\mu^+\mu^-} < 105$ GeV. The sample was collected with two triggers, a single muon trigger with $p_{\mathrm{T}} > 24$ GeV for the lower instantaneous luminosity part, and a single muon trigger with $p_{\mathrm{T}} > 36$ GeV for the higher instantaneous luminosity part of the sample. Muon tracks were required to be within the TRT pseudorapidity acceptance of $|\eta| < 2.0$ and have more than 15 TRT hits.

Some leading-edge time distributions are shown in Figures 8 and 9 for the TRT end-caps. The small differences between simulation and data in the shapes of these distributions are explained by the effect of the 40 MHz clock noise which leads to a slight modulation of the electronics base line and hence some time dependence of the effective threshold. This effect is not modeled in the simulation.

The position residual is defined as the difference between the measured drift-radius and the closest approach of the reconstructed track to the anode wire. The track position measurement accuracy is defined as the sigma of Gaussian fit to the core ($\pm$ 1.5σ) of the distributions shown in Figures 10-13. In these figures the position residual distribution is shown for the barrel and end-cap regions at low and high values of $\langle\mu\rangle$. The residual is well described by the simulation in the end-cap while in the barrel the simulation slightly underestimates the track position measurement accuracy. For the pp running during Run 1, depending on the p_{T} of the track, pseudorapidity, and the straw occupancy, the TRT track position measurement accuracy varies between 100 μm and 130 μm.

Figures 14 and 15 show the track position measurement accuracy versus η for low and high values of $\langle\mu\rangle$ comparing data and simulation. Figures 16-18 show the track position measurement accuracy as a function of $\langle\mu\rangle$ for the overall TRT and the barrel and end-cap separately for data compared to simulation. The simulation underestimates the track position measurement accuracy in the barrel by about 6 μm. In the end-cap the simulation is in very good agreement with the data.

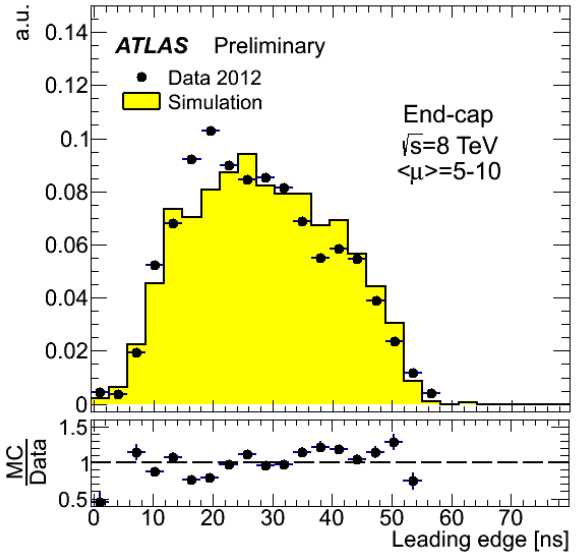

Figure 8: TRT end-cap leading-edge time distribution for $5 < \langle\mu\rangle < 10$. Data (closed circles) and simulation (histogram) are shown for 2012 running.

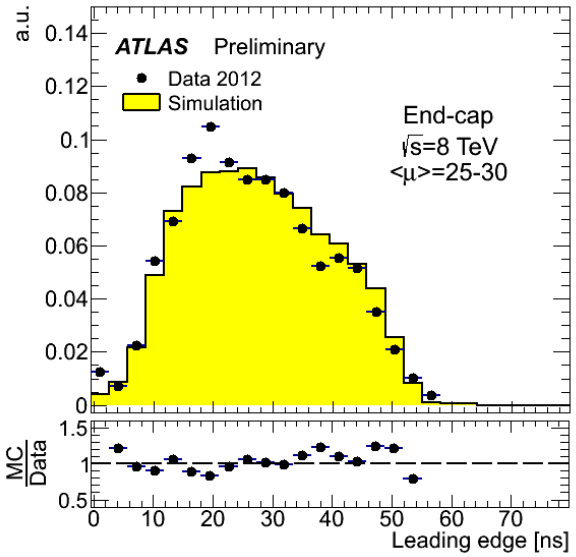

Figure 9: TRT end-cap leading-edge time distribution for $25 < \langle\mu\rangle < 30$. Data (closed circles) and simulation (histogram) are shown for 2012 running.

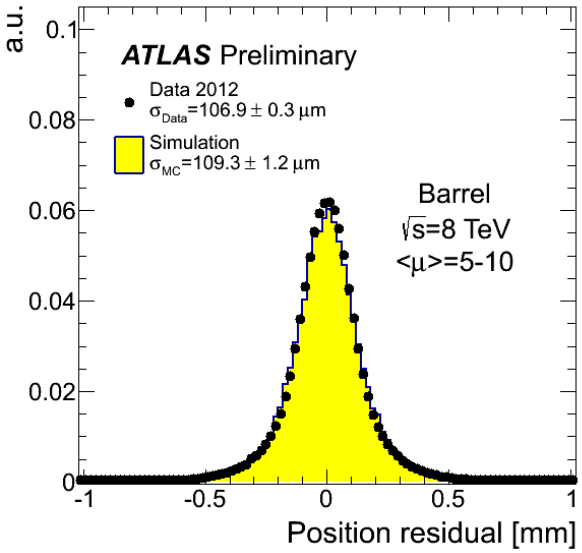

Figure 10: Position residual distribution in the TRT barrel for muons $p_{\mathrm{T}} > 30$ GeV. Data (solid circles) and simulation (histogram) are shown for 2012 running at $5 \leq \langle\mu\rangle \leq 10$.

The track position measurement accuracy is measured to be:
$\sigma_{Data} = 106.9 \pm 0.3\mu$m, $\sigma_{MC} = 109.3 \pm 1.2\mu$m.

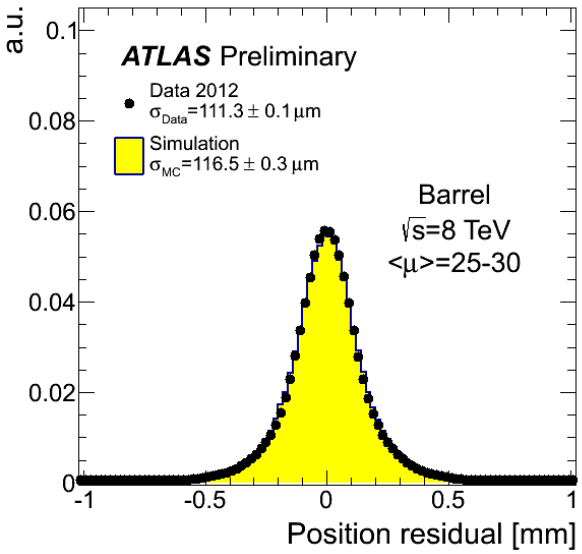

Figure 11: Position residual distribution in the TRT barrel for muons $p_{\mathrm{T}} > 30$ GeV. Data (solid circles) and simulation (histogram) are shown for 2012 running at $25 \leq \langle\mu\rangle \leq 30$.

The track position measurement accuracy is measured to be:
$\sigma_{Data} = 111.3 \pm 0.1\mu$m, $\sigma_{MC} = 116.5 \pm 0.3\mu$m.

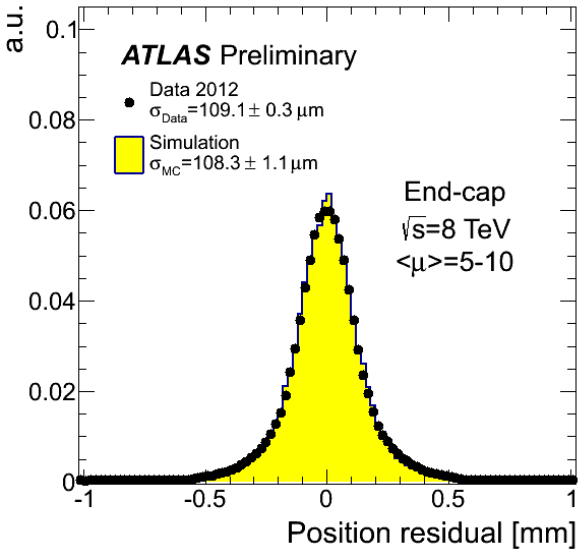

Figure 12: Position residual distribution in the TRT end-cap for muons $p_{\mathrm{T}} > 30$ GeV. Data (solid circles) and simulation (histogram) are shown for 2012 running at $5 \leq \langle\mu\rangle \leq 10$.

The track position measurement accuracy is measured to be:
$\sigma_{Data} = 109.1 \pm 0.3\mu$m, $\sigma_{MC} = 108.3 \pm 1.1\mu$m.

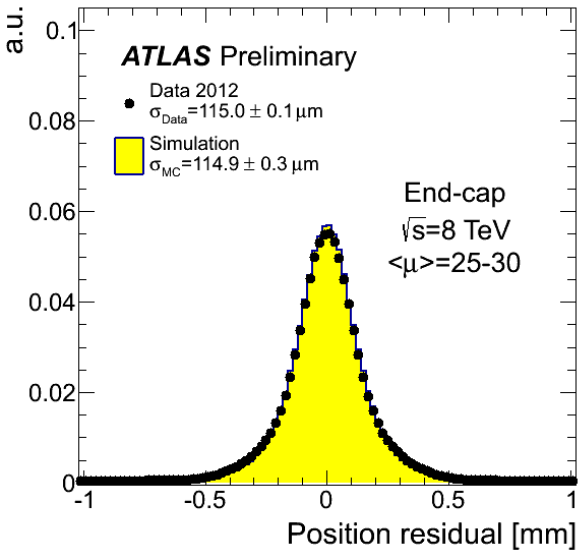

Figure 13: Position residual distribution in the TRT end-cap for muons $p_{\mathrm{T}} > 30$ GeV. Data (solid circles) and simulation (histogram) are shown for 2012 running at $25 \leq \langle\mu\rangle \leq 30$.

The track position measurement accuracy is measured to be:
$\sigma_{Data} = 115.0 \pm 0.1\mu$m, $\sigma_{MC} = 114.9 \pm 0.3\mu$m.

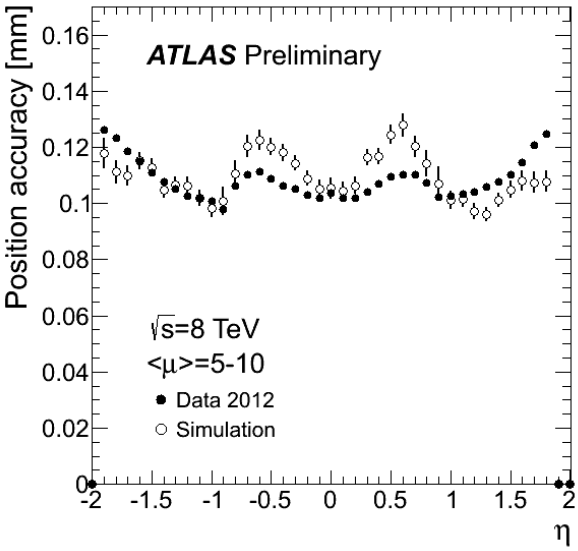

Figure 14: Track position measurement accuracy in the straw as a function of pseudorapidity (η) for muons $p_{\mathrm{T}} > 30$ GeV. Data (solid circles) and simulation (open circles) are shown for 2012 running at $5 \leq \langle\mu\rangle \leq 10$.

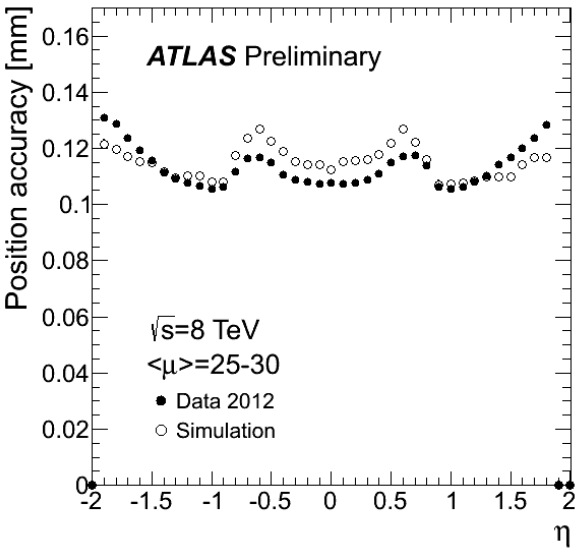

Figure 15: Track position measurement accuracy in the straw as a function of pseudorapidity (η) for muons $p_{\mathrm{T}} > 30$ GeV. Data (solid circles) and simulation (open circles) are shown for 2012 running at $25 \leq \langle\mu\rangle \leq 30$.

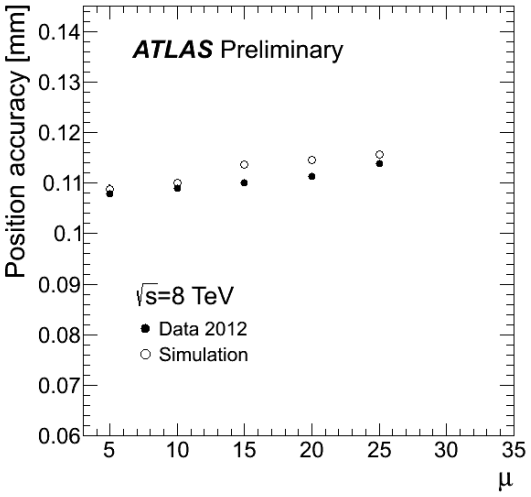

Figure 16: Track position measurement accuracy in the straw for muons $p_{\mathrm{T}} > 30$ GeV in the entire TRT as a function of the average number of interactions ($\langle\mu\rangle$). Data (solid circles) and simulation (open circles) are shown for 2012 running where the average number of interactions per bunch crossing varied with $5 \leq \langle\mu\rangle \leq 30$.

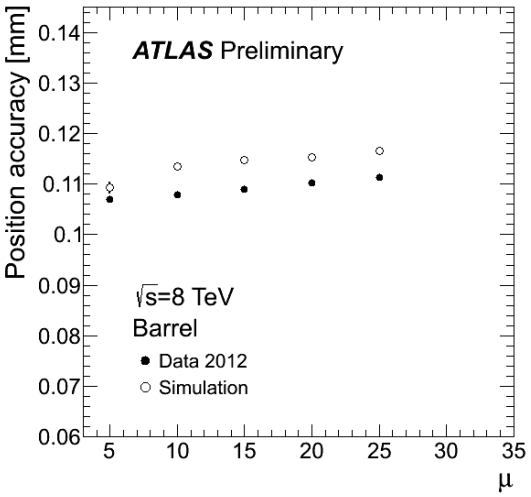

Figure 17: Track position measurement accuracy in the straw for muons $p_{\mathrm{T}} > 30$ GeV in the TRT barrel as a function of the average number of interactions ($\langle\mu\rangle$). Data (solid circles) and simulation (open circles) are shown for 2012 running where the average number of interactions per bunch crossing varied with $5 \leq \langle\mu\rangle \leq 30$.

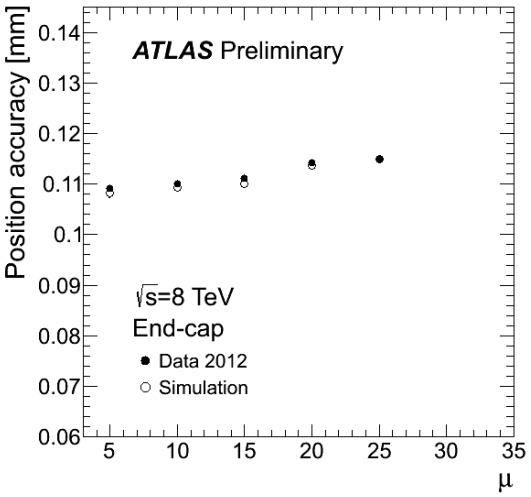

Figure 18: Track position measurement accuracy in the straw for muons $p_{\mathrm{T}} > 30$ GeV in the TRT end-cap as a function of the average number of interactions ($\langle\mu\rangle$). Data (solid circles) and simulation (open circles) are shown for 2012 running where the average number of interactions per bunch crossing varied with $5 \leq \langle\mu\rangle \leq 30$.

4 High threshold probability for minimum-ionizing particles

Electron identification is based on the ratio of high level hits to low level hits on a track. At the straw level in the region of interest (pseudorapidity or straw layer), the "high level hit probability" is defined as the average ratio of the total number of high level hits to the total number of low level hits on the straws associated to particle tracks.

This section presents results for the measurement of the probability for muons to generate enough ionization energy to exceed the high threshold. Plots are prepared using tracks from two decay channels to muons (J/ψ and Z) and in two momentum ranges (low and high) to verify that the agreement between simulation and data extends to a variety of kinematic conditions.

The J/ψ decay muons have $5 < p < 20$ GeV, the majority being still on the Bethe-Bloch formula relativistic rise, while the Z decay muons, having a typical momentum greater than 30 GeV, are placed well on the ionization loss plateau (no low energy muons are present in this sample). An upper cut of $p < 60$ GeV is placed on these muons. The amount of ionization deposited by the higher energy muons is slightly larger on average and consequently the high threshold probability is slightly increased.

The muons in both samples have momenta below the momentum needed to produce transition radiation (~60 GeV, corresponding to a Lorentz γ-factor of ~600). The high threshold hits are therefore the result of ionization above ≈6 keV which is significantly higher than the average energy deposited by a muon (≈2.5 keV). Such hits represent an irreducible background to the electron identification by high threshold hits caused by a combination of ionization losses and absorbed transition radiation X-ray photons.

The use of muons from the $J/\psi \rightarrow \mu^+\mu^-$ and $Z \rightarrow \mu^+\mu^-$ peaks provides high purity samples of low energy muons with no electron contamination. The selected momentum range of this sample covers the momentum range where the TRT contributes most significantly to improve the electron identification provided by the electromagnetic calorimeter.

The data samples used were from the 2011 running period which were taken with 50 ns bunch spacing and at a low number of interactions per bunch crossing ($3 < \langle\mu\rangle < 9$). Cuts of $\Delta R > 0.3$ on the angle between the decay muons and $p_{\mathrm{T}} > 5$ GeV were used. The J/ψ sample required a trigger with two muons with $p_{\mathrm{T}} > 4$ GeV and with $3.0 < M_{\mu^+\mu^-} < 3.2$ GeV. The Z sample required a single muon trigger with $p_{\mathrm{T}} > 18$ GeV and a di-muon mass $75 < M_{\mu^+\mu^-} < 105$ GeV.

Figures 19 and 20 show the probability of a hit from a muon track passing the high threshold as function of η for muons from J/ψ and Z decays; data and simulation are in good agreement. Figures 21 and 22 show the probability for a TRT hit on a muon track to exceed the high threshold versus barrel straw layer number. The TRT barrel straws are numbered from 1 (innermost radially) to 73 (outermost radially). It can be seen that for the innermost part of the TRT, where the charged particle density is highest, the probability of recording a high threshold hit is highest. As the charged particle fluence decreases with increasing radius from the beam axis, the high threshold hit probability decreases.

Figures 23-26 show the probability for a TRT hit on a muon track to exceed the high threshold versus end-cap straw layer number. The TRT end-cap straws are numbered from 1 (nearest in z to the IP) to 160 (furthest in z from the IP). The data is nearly flat as function of Z while the simulation has The difference in the slope between simulation and data can be explained by the fact that in the simulation the threshold is set to the same value for all straws and, because of the change in the incident angle, dE/dx in straws has a dependence on straw layer. However in the data, the high threshold is tuned to equalize high threshold probability along straw layers.

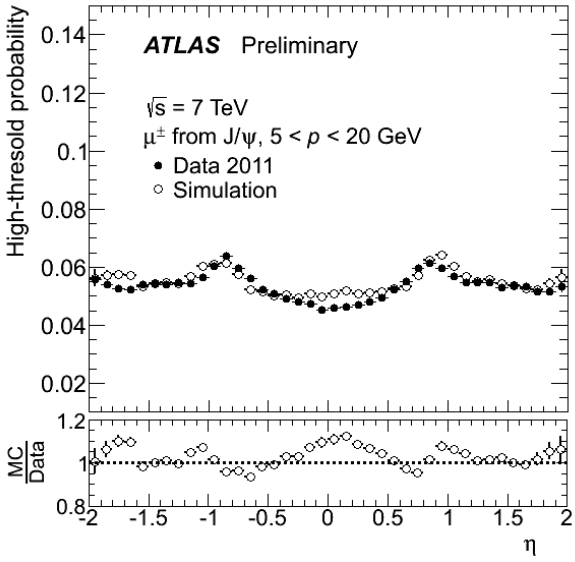

Figure 19: The probability for a TRT hit on a muon track to exceed the TRT high threshold as a function of the track pseudorapidity (η). Muons from the channel $J/\psi \rightarrow \mu^+\mu^-$ with $5 < p < 20$ GeV are used. Data (solid circles) and simulation (open circles) are shown for 2011 running at $\sqrt{s} = 7$ TeV with $3 < \langle\mu\rangle < 9$.

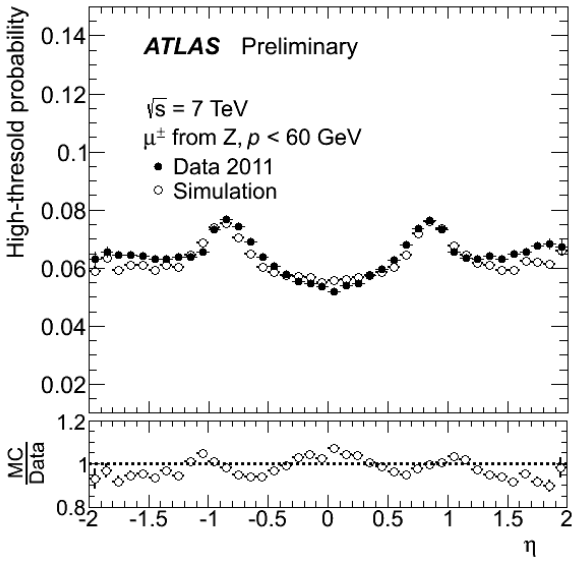

Figure 20: The probability for a TRT hit on a muon track to exceed the TRT high threshold as a function of the track pseudorapidity (η). Muons from the channel $Z \rightarrow \mu^+\mu^-$ with $p < 60$ GeV are used. Data (solid circles) and simulation (open circles) are shown for 2011 running at $\sqrt{s} = 7$ TeV with $3 < \langle\mu\rangle < 9$.

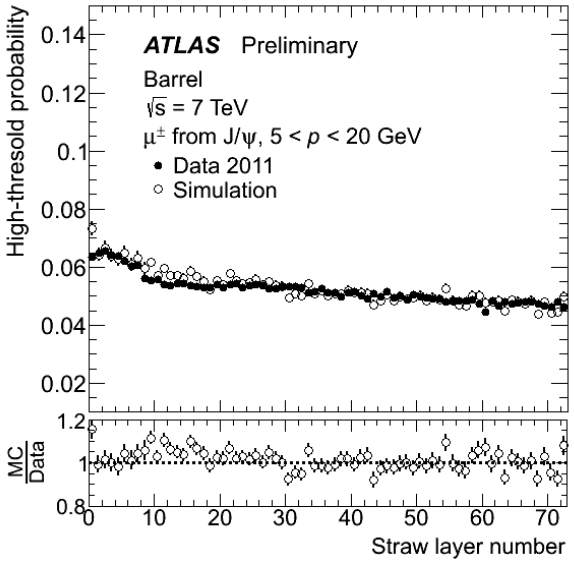

Figure 21: The probability for a TRT hit on a muon track to exceed the TRT high threshold as a function of the barrel straw layer. Muons from the channel $J/\psi \rightarrow \mu^+\mu^-$ with $5 < p < 20$ GeV are used. Data (solid circles) and simulation (open circles) are shown for 2011 running at $\sqrt{s} = 7$ TeV with $3 < \langle\mu\rangle < 9$. The first 9 layers have a shorter straw length which leads to slightly higher signals and in turn to a higher high level threshold probability. For the long straws the high threshold probability declines slightly with increasing layer radius.

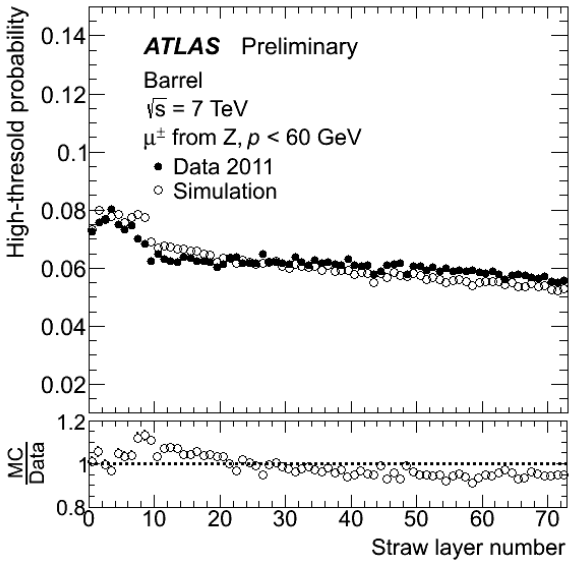

Figure 22: The probability for a TRT hit on a muon track to exceed the TRT high threshold as a function of the barrel straw layer. Muons from the channel $Z \rightarrow \mu^+\mu^-$ with $p < 60$ GeV are used. Data (solid circles) and simulation (open circles) are shown for 2011 running at $\sqrt{s} = 7$ TeV with $3 < \langle\mu\rangle < 9$. The first 9 layers have a shorter straw length which leads to slightly higher signals and in turn to a higher high level threshold probability. For the long straws the high threshold probability declines slightly with increasing layer radius.

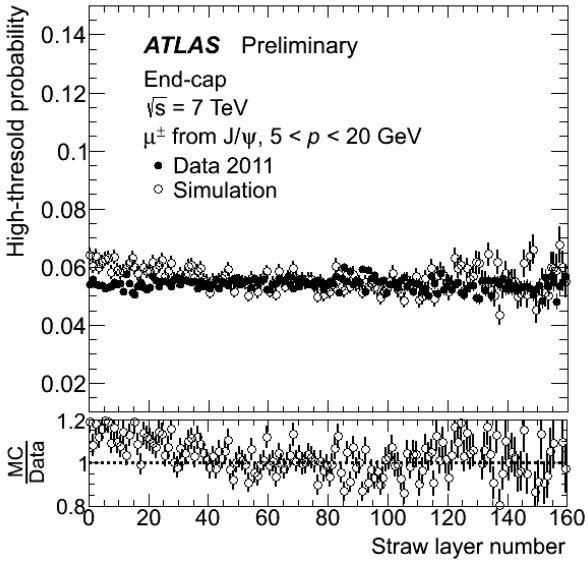

Figure 23: The probability for a TRT hit on a muon track to exceed the TRT high threshold as a function of the end-cap straw layer. Muons from the channel $J/\psi \rightarrow \mu^+\mu^-$ with $5 < p < 20$ GeV are used. Data (solid circles) and simulation (open circles) are shown for 2011 running at $\sqrt{s} = 7$ TeV with $3 < \langle\mu\rangle < 9$.

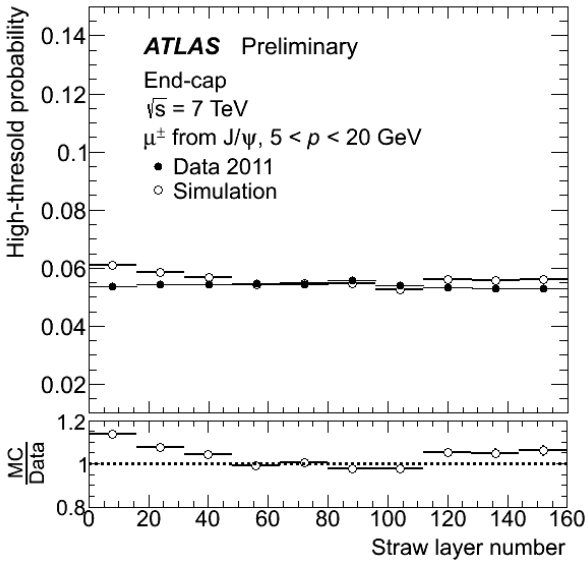

Figure 24: The probability for a TRT hit on a muon track to exceed the TRT high threshold as a function of the end-cap straw layer, binned into groups of sixteen straw layers. Muons from the channel $J/\psi \rightarrow \mu^+\mu^-$ with $5 < p < 20$ GeV are used. Data (solid circles) and simulation (open circles) are shown for 2011 running at $\sqrt{s} = 7$ TeV with $3 < \langle\mu\rangle < 9$.

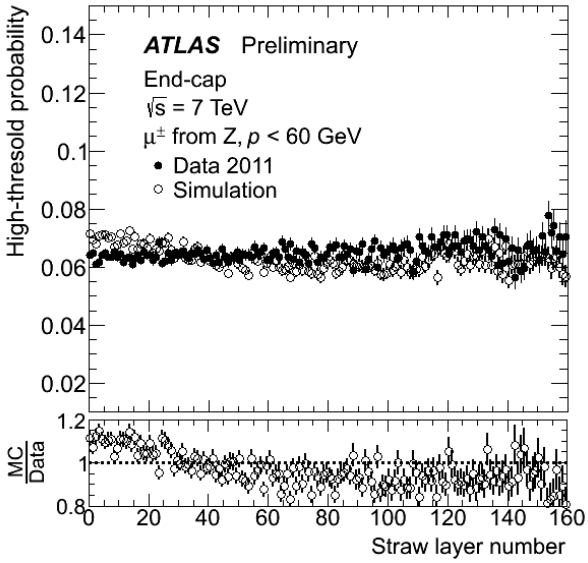

Figure 25: The probability for a TRT hit on a muon track to exceed the TRT high threshold as a function of the end-cap straw layer. Muons from the channel $Z \rightarrow \mu^+\mu^-$ with $p < 60$ GeV are used. Data (solid circles) and simulation (open circles) are shown for 2011 running at $\sqrt{s} = 7$ TeV with $3 < \langle\mu\rangle < 9$.

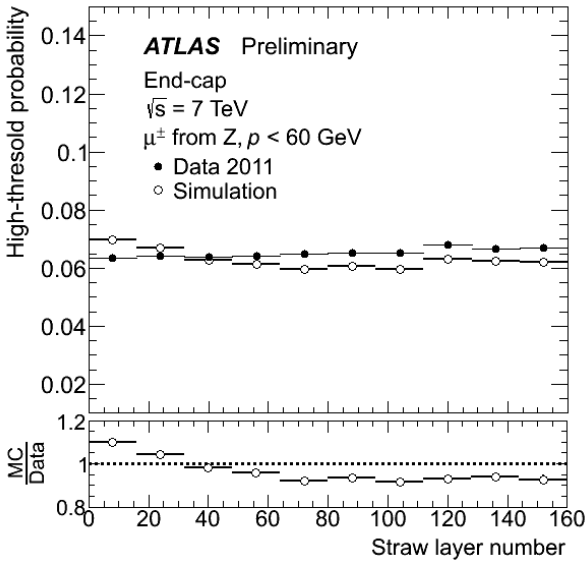

Figure 26: The probability for a TRT hit on a muon track to exceed the TRT high threshold as a function of the end-cap straw layer, binned into groups of sixteen straw layers. Muons from the channel $Z \rightarrow \mu^+\mu^-$ with $p < 60$ GeV are used. Data (solid circles) and simulation (open circles) are shown for 2011 running at $\sqrt{s} = 7$ TeV with $3 < \langle\mu\rangle < 9$.

5 High threshold probability for electrons

This section presents results for the measurement of the probability for electrons to generate enough ionization energy to exceed the high threshold producing an electron-identifying signal. Plots are prepared using tracks from different decays (J/ψ and Z) and in different momentum ranges (low and high) to verify that the agreement between simulation and data extends to a variety of kinematic conditions.

The electrons in both samples have momenta well above the momentum needed to produce transition radiation (~0.5 GeV, corresponding to a Lorentz γ-factor of ~1000). While the absorption of transition radiation X-rays in Xenon is by far the dominant contribution, a significant contribution to high threshold comes also from dE/dx (≈25% of the total).

The selected runs and cuts used for this analysis created a pure sample of electrons. The data samples used were from the 2011 running period which were taken with 50 ns bunch spacing and at a low number of interactions per bunch crossing ($3 < \langle\mu\rangle < 9$).

For J/ψ decays, both electrons are required to fulfill `Medium++` identification requirements [8], have $p_{\mathrm{T}} > 5$ GeV, $|\eta| < 2.0$, and have at least one hit in the pixel detector associated. The two electrons must be separated from each other by $\Delta R > 0.2$, have opposite charges and an invariant mass between 2.9 and 3.2 GeV.

For Z decays, one electron must fulfill the strict `Tight++` electron identification requirements, have $p_{\mathrm{T}} > 22$ GeV and be isolated in the calorimeter by $E_T^{cone-0.4} < 6$ GeV. The other electron must fulfill the `Loose++` identification criteria, and have $p_{\mathrm{T}} > 15$ GeV. The two electrons must have a separation of $\Delta R > 0.3$, have opposite electric charges and their invariant mass must be between 75 and 105 GeV. Only the electron fulfilling the `Loose++` identification criteria is used for the studies.

Figures 27 to 30 show the probability for a hit from electrons to pass the high threshold versus η for data and simulation. The probability is about 21% in the central region and increases to about 35% at the highest η values. The data are well described by the simulation. Figures 31 to 34 show the probability versus straw layer number in the barrel, and Figures 35 and 42 show it in the end-cap. At higher momentum, the high threshold probability is seen to be larger; this reflects the fact that TR yield is still rising with electron energy.

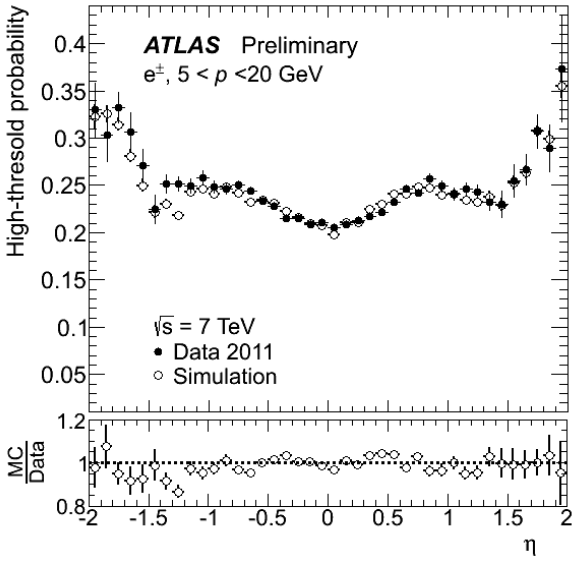

Figure 27: The probability for a TRT hit from an electron track to exceed the TRT high threshold as a function of the track pseudorapidity (η). Electrons from the channel Z and $J/\psi \rightarrow e^+e^-$ with $5 < p < 20$ GeV are used. Data (solid circles) and simulation (open circles) are shown for 2011 running at $\sqrt{s} = 7$ TeV with $3 < \langle\mu\rangle < 9$.

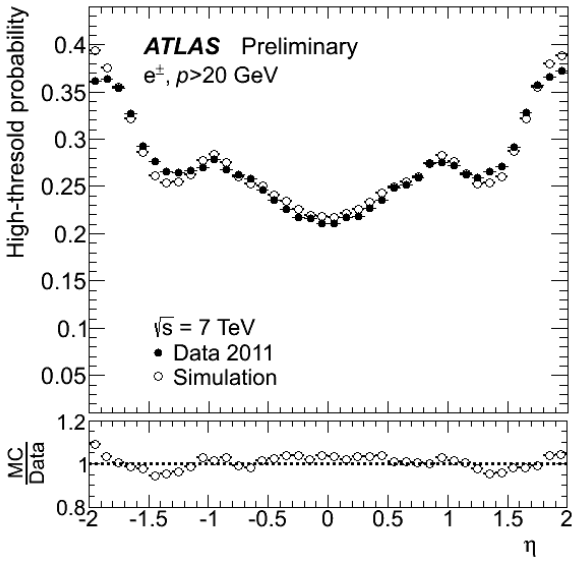

Figure 28: The probability for a TRT hit from an electron track to exceed the TRT high threshold as a function of the track pseudorapidity (η). Electrons from the channel Z and $J/\psi \rightarrow e^+e^-$ with $p > 20$ GeV are used. Data (solid circles) and simulation (open circles) are shown for 2011 running at $\sqrt{s} = 7$ TeV with $3 < \langle\mu\rangle < 9$.

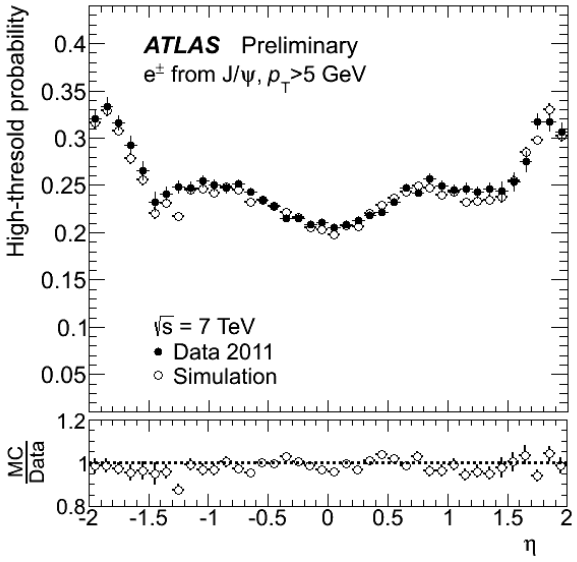

Figure 29: The probability for a TRT hit from an electron track to exceed the TRT high threshold as a function of the track pseudorapidity (η). Electrons from the channel $J/\psi \rightarrow e^+e^-$ with $p_{\mathrm{T}} > 5$ GeV are used. Data (solid circles) and simulation (open circles) are shown for 2011 running at $\sqrt{s} = 7$ TeV with $3 < \langle\mu\rangle < 9$.

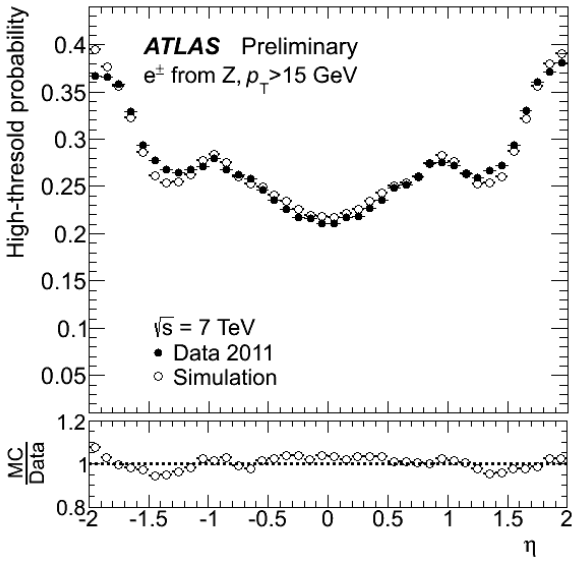

Figure 30: The probability for a TRT hit from an electron track to exceed the TRT high threshold as a function of the track pseudorapidity (η). Electrons from the channel $Z \rightarrow e^+e^-$ with $p_{\mathrm{T}} > 15$ GeV are used. Data (solid circles) and simulation (open circles) are shown for 2011 running at $\sqrt{s} = 7$ TeV with $3 < \langle\mu\rangle < 9$.

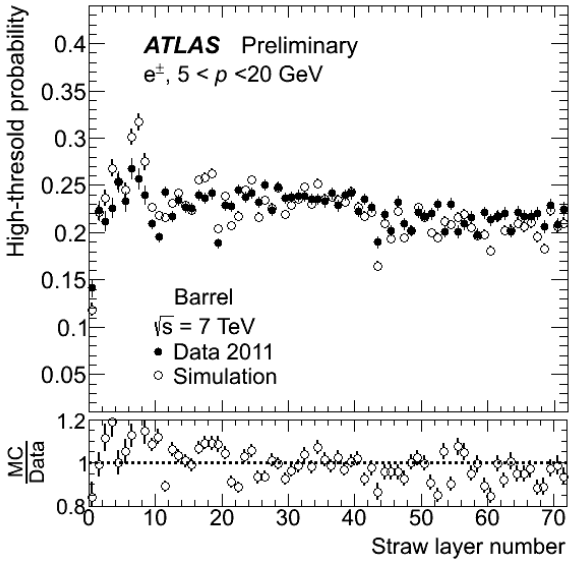

Figure 31: The probability for a TRT hit from an electron track to exceed the TRT high threshold as a function of the barrel straw layer. Electrons from the channels Z and $J/\psi \rightarrow e^+e^-$ with $5 < p < 20$ GeV are used. Data (solid circles) and simulation (open circles) are shown for 2011 running at $\sqrt{s} = 7$ TeV with $3 < \langle\mu\rangle < 9$.

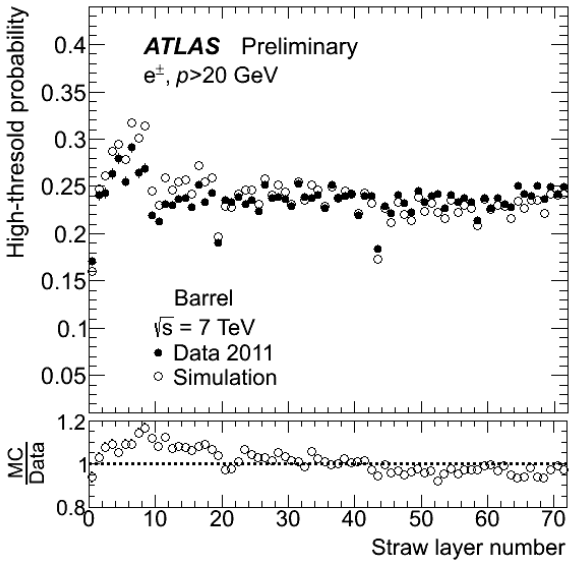

Figure 32: The probability for a TRT hit on a electron track to exceed the TRT high threshold as a function of the barrel straw layer. Electrons from the channels Z and $J/\psi \rightarrow e^+e^-$ with $p > 20$ GeV are used. Data (solid circles) and simulation (open circles) are shown for 2011 running at $\sqrt{s} = 7$ TeV with $3 < \langle\mu\rangle < 9$.

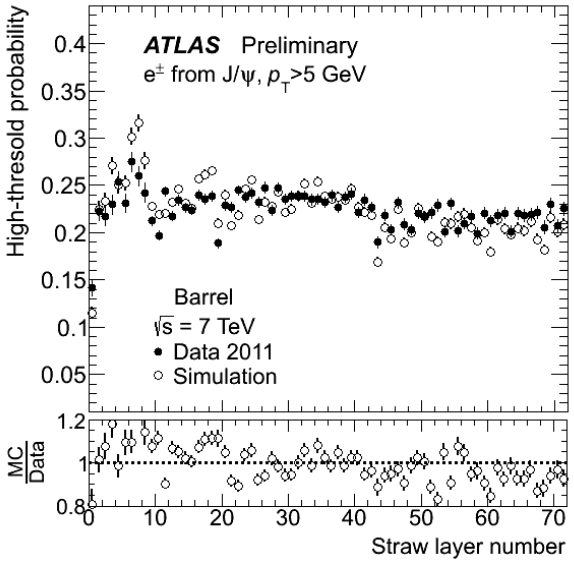

Figure 33: The probability for a TRT hit on an electron track to exceed the TRT high threshold as a function of the barrel straw layer. Electrons from the channel $J/\psi \rightarrow e^+e^-$ with $p_{\mathrm{T}} > 5$ GeV are used. Data (solid circles) and simulation (open circles) are shown for 2011 running at $\sqrt{s} = 7$ TeV with $3 < \langle\mu\rangle < 9$.

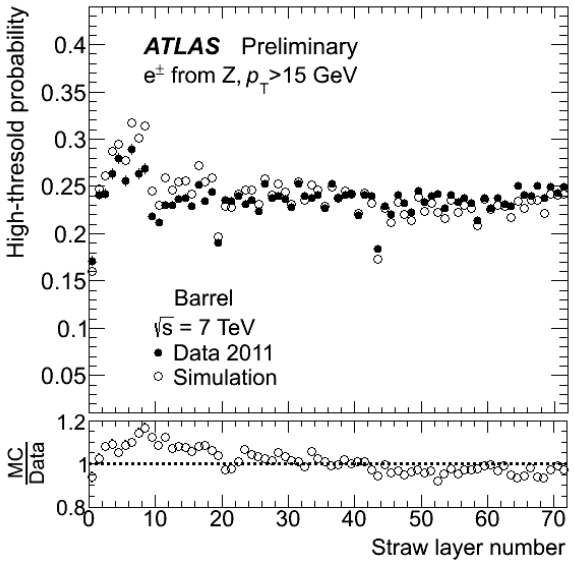

Figure 34: The probability for a TRT hit on an electron track to exceed the TRT high threshold as a function of the barrel straw layer. Electrons from the channel $Z \rightarrow e^+e^-$ with $p_{\mathrm{T}} > 15$ GeV are used. Data (solid circles) and simulation (open circles) are shown for 2011 running at $\sqrt{s} = 7$ TeV with $3 < \langle\mu\rangle < 9$.

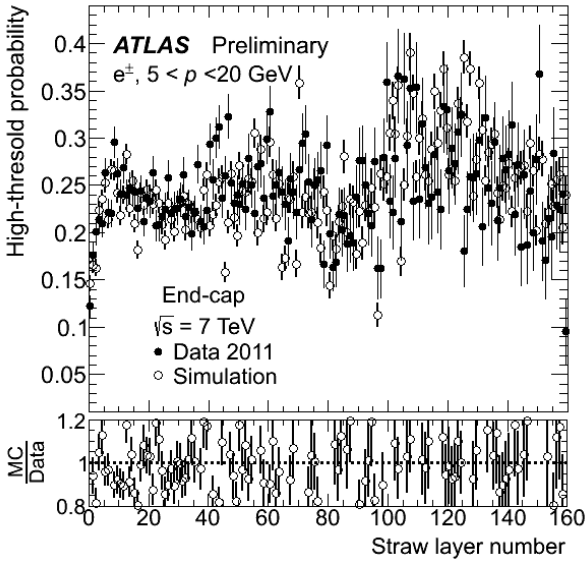

Figure 35: The probability for a TRT hit on an electron track to exceed the TRT high threshold as a function of the end-cap straw layer. Electrons from the channels Z and $J/\psi \rightarrow e^+e^-$ with $5 < p < 20$ GeV are used. Data (solid circles) and simulation (open circles) are shown for 2011 running at $\sqrt{s} = 7$ TeV with $3 < \langle\mu\rangle < 9$.

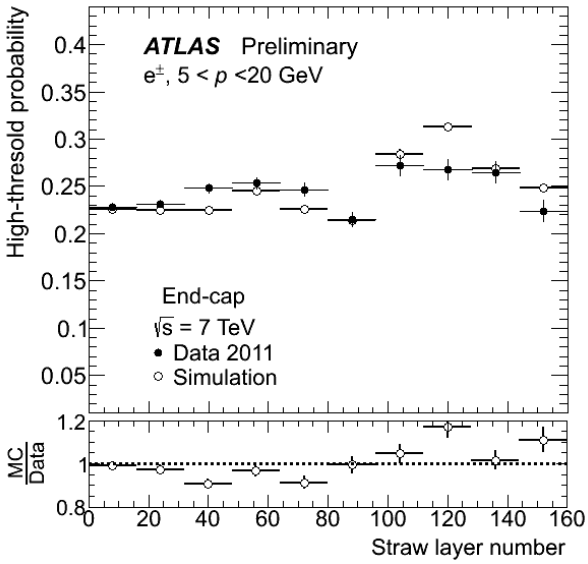

Figure 36: The probability for a TRT hit on an electron track to exceed the TRT high threshold as a function of the end-cap straw layer, binned into groups of sixteen straw layers. Electrons from the channels Z and $J/\psi \rightarrow e^+e^-$ with $5 < p < 20$ GeV are used. Data (solid circles) and simulation (open circles) are shown for 2011 running at $\sqrt{s} = 7$ TeV with $3 < \langle\mu\rangle < 9$.

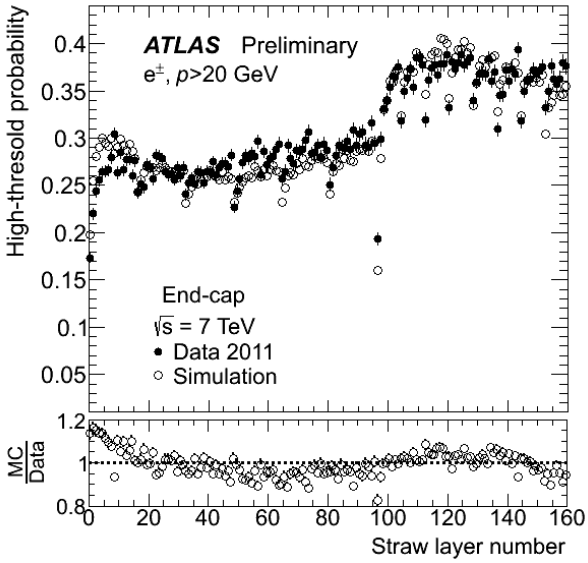

Figure 37: The probability for a TRT hit on an electron track to exceed the TRT high threshold as a function of the end-cap straw layer. Electrons from the channels Z and $J/\psi \rightarrow e^+e^-$ with $p > 20$ GeV are used. Data (solid circles) and simulation (open circles) are shown for 2011 running at $\sqrt{s} = 7$ TeV with $3 < \langle\mu\rangle < 9$.

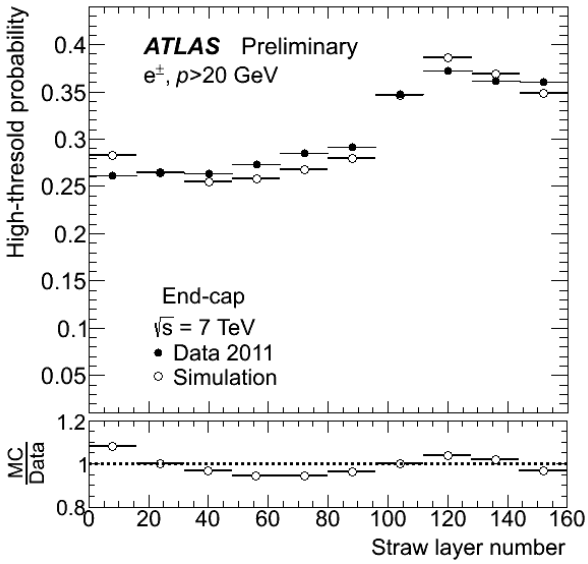

Figure 38: The probability for a TRT hit on an electron track to exceed the TRT high threshold as a function of the end-cap straw layer, binned into groups of sixteen straw layers. Electrons from the channels Z and $J/\psi \rightarrow e^+e^-$ with $p > 20$ GeV are used. Data (solid circles) and simulation (open circles) are shown for 2011 running at $\sqrt{s} = 7$ TeV with $3 < \langle\mu\rangle < 9$.

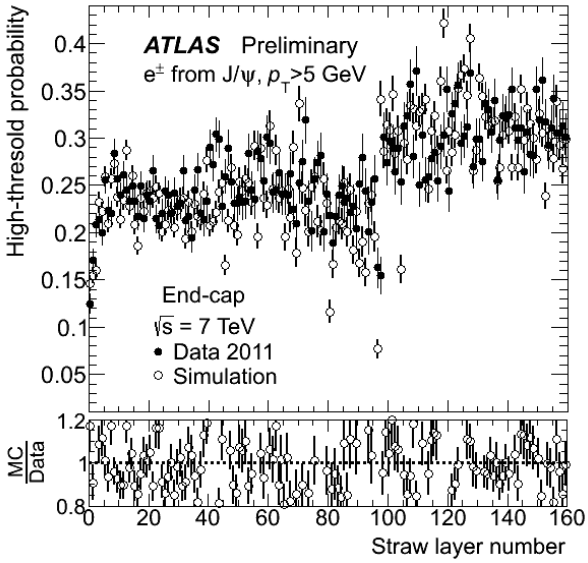

Figure 39: The probability for a TRT hit on an electron track to exceed the TRT high threshold as a function of the end-cap straw layer. Electrons from the channel $J/\psi \rightarrow e^+e^-$ with $p_{\mathrm{T}} > 5$ GeV are used. Data (solid circles) and simulation (open circles) are shown for 2011 running at $\sqrt{s} = 7$ TeV with $3 < \langle\mu\rangle < 9$.

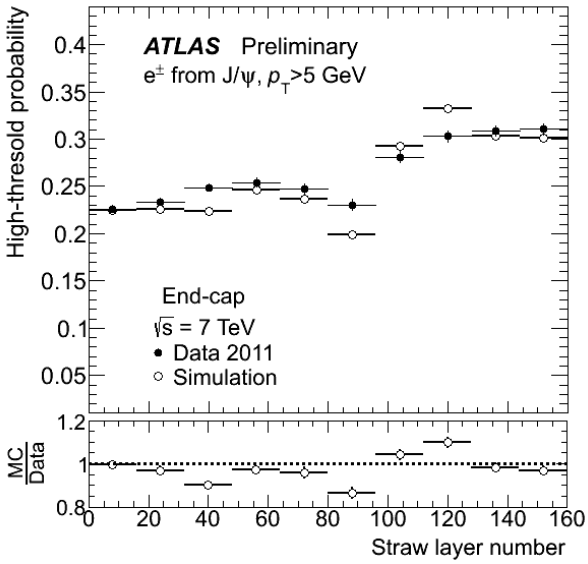

Figure 40: The probability for a TRT hit on an electron track to exceed the TRT high threshold as a function of the end-cap straw layer, binned into groups of sixteen straw layers. Electrons from the channel $J/\psi \rightarrow e^+e^-$ with $p_{\mathrm{T}} > 5$ GeV are used. Data (solid circles) and simulation (open circles) are shown for 2011 running at $\sqrt{s} = 7$ TeV with $3 < \langle\mu\rangle < 9$.

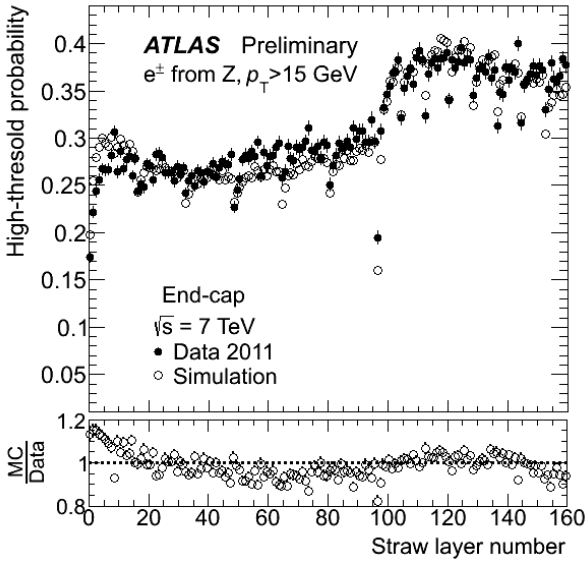

Figure 41: The probability for a TRT hit on an electron track to exceed the TRT high threshold as a function of the end-cap straw layer. Electrons from the channel $Z \rightarrow e^+e^-$ with $p_{\mathrm{T}} > 15$ GeV are used. Data (solid circles) and simulation (open circles) are shown for 2011 running at $\sqrt{s} = 7$ TeV with $3 < \langle\mu\rangle < 9$.

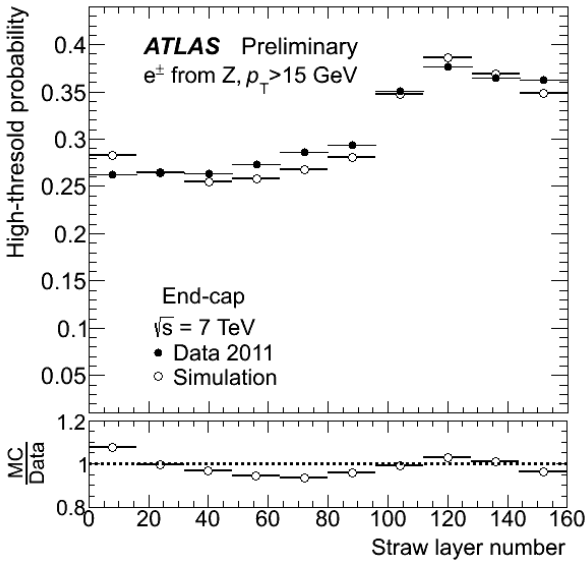

Figure 42: The probability for a TRT hit on an electron track to exceed the TRT high threshold as a function of the end-cap straw layer, binned into groups of sixteen straw layers. Electrons from the channel $Z \rightarrow e^+e^-$ with $p_{\mathrm{T}} > 15$ GeV are used. Data (solid circles) and simulation (open circles) are shown for 2011 running at $\sqrt{s} = 7$ TeV with $3 < \langle\mu\rangle < 9$.

6 High threshold probability as a function of Lorentz γ-factor

The measurements for electrons and muons described in the previous section are combined, and probabilities to exceed high level threshold versus the particle Lorentz γ-factor are presented here. The p_{T} cuts are relaxed to extend the coverage of the Lorentz γ-factor. All electron tracks have sufficiently high γ-factors to generate TR. Only the most energetic muons have large enough γ-factors to emit transition radiation; these muons are useful for mapping the turn-on of the transition radiation.

The service region between the barrel and end-cap has lowest pion rejection power because of the large volume of service material which reduces the number of possible high threshold hits on tracks. Tracks also create showers in the service region and lose energy. The best region for pion rejection is the boundary region spanning the type A and type B wheels where the tracks cross the maximum number of radiator layers and have the largest number of measurements. The other three regions have pion rejection factors in between these two extremes.

Figures 43-47 show the probability of a hit to pass the high threshold versus the Lorentz γ-factor for five η ranges. In all cases electrons and muons from both J/ψ and Z decays are shown for data and simulation. As expected, a turn-on of TR is seen to occur in the γ-factor range 10^3-10^4. The simulation agrees well with the data.

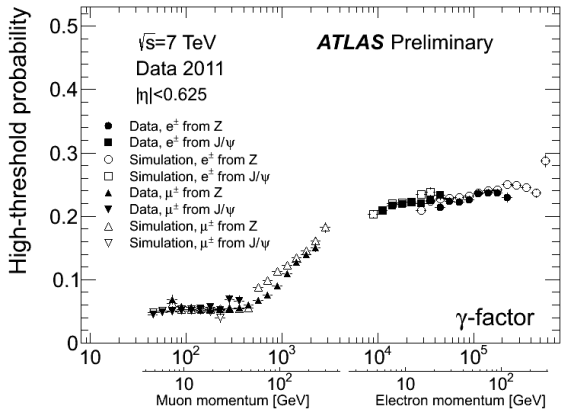

Figure 43: The probability to exceed the high threshold for electrons and muons from J/ψ and Z decays as a function of the Lorentz γ-factor for tracks with $|\eta| < 0.625$ corresponding to the TRT barrel region. Data (solid symbols) and simulation (open symbols) are shown for low luminosity running during 2011.

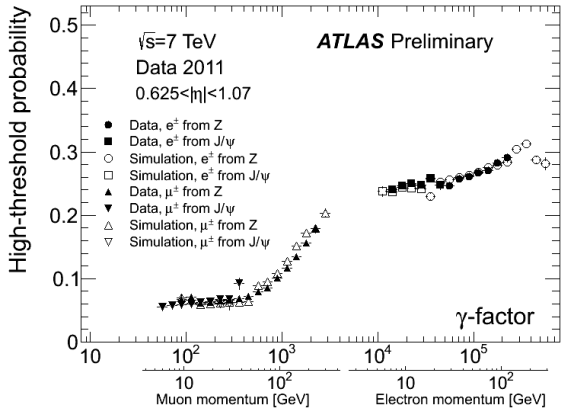

Figure 44: The probability to exceed the high threshold for electrons and muons from J/ψ and Z decays as a function of the Lorentz γ-factor for tracks with $0.625 < |\eta| < 1.070$ corresponding to the service crack region between the TRT barrel and end-cap regions. Data (solid symbols) and simulation (open symbols) are shown for low luminosity running during 2011.

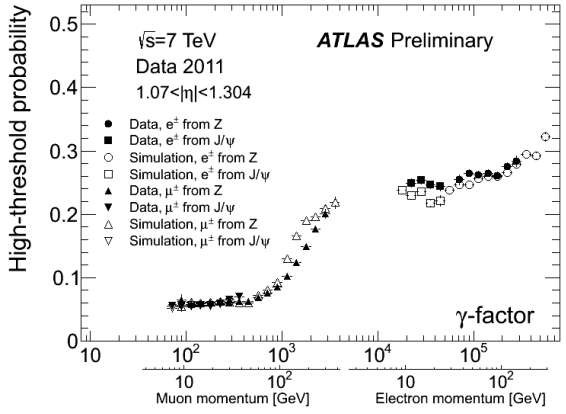

Figure 45: The probability to exceed the high threshold for electrons and muons from J/ψ and Z decays as a function of the Lorentz γ-factor for tracks with $1.070 < |\eta| < 1.304$ corresponding to the TRT type A end-cap wheel region. Data (solid symbols) and simulation (open symbols) are shown for low luminosity running during 2011.

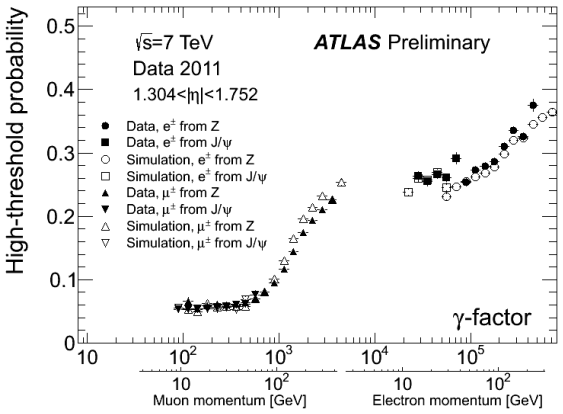

Figure 46: The probability to exceed the high threshold for electrons and muons from J/ψ and Z decays as a function of the Lorentz γ-factor for tracks with $1.304 < |\eta| < 1.752$ corresponding to the boundary region between the TRT type A and type B end-cap wheels. Data (solid symbols) and simulation (open symbols) are shown for low luminosity running during 2011.

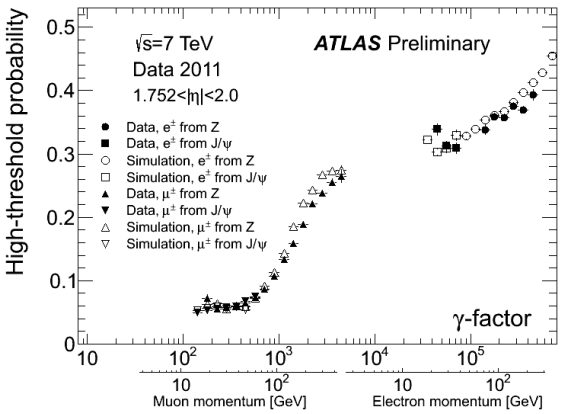

Figure 47: The probability to exceed the high threshold for electrons and muons from J/ψ and Z decays as a function of the Lorentz γ-factor for tracks with $1.752 < |\eta| < 2.0$ corresponding to the TRT type B end-cap wheel region. Data (solid symbols) and simulation (open symbols) are shown for low luminosity running during 2011.

7 Occupancy as a function of interactions per bunch crossing

This section presents the TRT straw occupancy as a function of $\langle\mu\rangle$ (up to 70) for a special run with "fat bunches" taken in 2012. In this run the distance between bunches was large resulting in no pile-up from adjacent bunches. Figures 48 and 49 show the occupancy as function of $\langle\mu\rangle$ separately for the barrel and the end-cap. Here occupancy is defined as the probability to have a low level (low threshold) hit within the 75 ns readout window. For each region, the occupancy is calculated as the number of straws with a low level discriminator fired during the 75 ns readout window divided by the total number of straws in the region. An allowance of 2.5% is made for permanently dead straws, and straws that are always on ("noisy straws") are not counted. The plots show that simulation describes well the dependence of the occupancy on the pile-up.

The occupancy increases linearly from about 24% at $\langle\mu\rangle$=45 to 35% at $\langle\mu\rangle$=70. The $\langle\mu\rangle$ values expected for Run 2 are about 25-40 and it is expected that there is no significant performance loss in this pile-up range in spite of a worsening of the TRT hit residual in higher occupancy events.

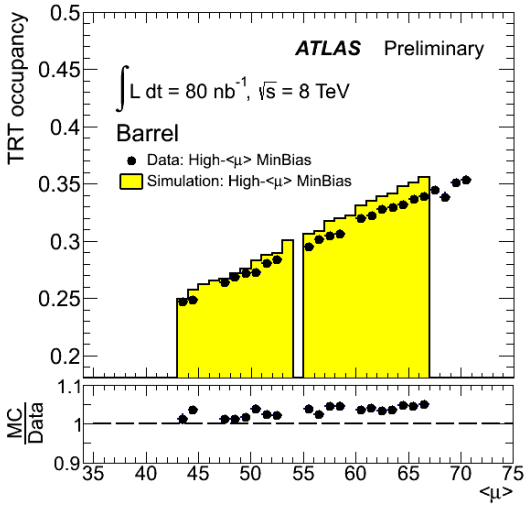

Figure 48: TRT straw occupancy as a function of $\langle\mu\rangle$ in the barrel for "fat bunch" runs (no pile-up from adjacent bunches) during 2012 at $\sqrt{s}$ = 8 TeV. Data (solid circles) and simulation (filled histograms).

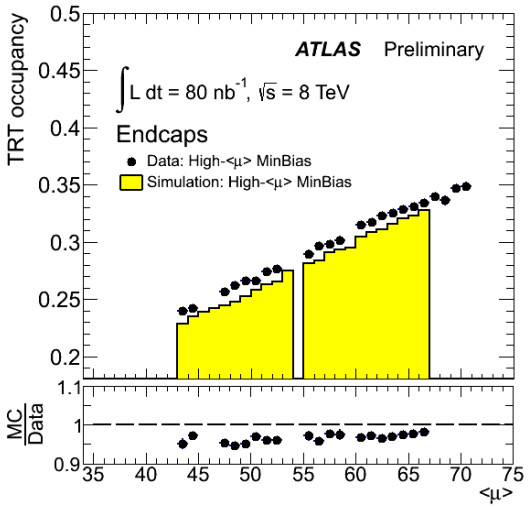

Figure 49: TRT straw occupancy as a function of $\langle\mu\rangle$ in the end-cap for "fat bunch" runs (no pile-up from adjacent bunches) during 2012 at $\sqrt{s}$ = 8 TeV. Data (solid circles) and simulation (filled histograms).

8 Tracking inside of jets at high pile-up

One of the most challenging environments for any tracking detector is finding and measuring tracks in the dense environment of energetic jet cores, particularly in the presence of high straw occupancy from pile-up events.

The primary standard ATLAS track-finding algorithm finds tracks first in the precision trackers (the Pixel and SCT detectors) and adds TRT hits to extend the track out to the calorimeter region. The study in this section looked at how TRT tracking properties change as a function of the distance of the track to the core of the jet (ΔR). The bins used are 0.02 wide in units of ΔR.

As in Section 7, this study used data from the "fat bunch" high pile-up runs taken at the end of the 2012 running period. TRT occupancy in these runs ranged between 10% and 50% with an average value of 30%.

The jets used for the study were restricted to the pseudorapidity range of the TRT acceptance ($|\eta| < 2.0$), and the lowest p_{T} jet was excluded if $\Delta R(jet1/jet2) < 0.8$. The tracks used for the study were selected using the following cuts: at least one pixel hit, at least five SCT hits, pseudorapidity restricted to the TRT acceptance ($|\eta| < 2.0$), transverse primary vertex constraint of 1.5 mm, and longitudinal primary vertex constraint of 1.5 mm, and a modest transverse momentum cut of 2 GeV.

Figures 50-57 show various Inner Detector and TRT related quantities for the following three jet p_{T} ranges:

- $30 < p_{\mathrm{T}} < 80$ GeV - less dense with easier track finding,
- $110 < p_{\mathrm{T}} < 160$ GeV - denser with more difficult track finding,
- $200 < p_{\mathrm{T}} < 400$ GeV - dense with challenging track finding.

In Figure 50 the number of tracks reconstructed by the ATLAS Inner Detector as a function of ΔR in jet cores is presented for the three jet p_{T} ranges. No requirement on the track TRT extension is applied. The track density increases almost by one order of magnitude in the central region of high p_{T} jets. Data and simulation are in quite good agreement.

Figure 51 shows the p_{T} sum of all reconstructed tracks in the Inner Detector for the three jet p_{T} ranges as a function of ΔR in the jet cores. One notes that an increase of total momentum in the area close to the center of jets is larger than the increase of total number of tracks; this reflects an increase of track p_{T} in the central region of jets. Simulation agrees well with data.

One of the important questions to be answered is how the TRT extension fraction inside of jets depends on distance to the core. Figure 52 shows the TRT track extension fraction as a function of ΔR in jet cores averaged over all $\langle\mu\rangle$. The track extension fraction reflects the relative number of tracks in which a track reconstructed in the Pixel and SCT detectors have a continuation (extension) in the TRT. The plot shows that the TRT track extension fraction is practically constant even within the dense cores of the most energetic jets. Data and simulation are in reasonable agreement. TRT extension fractions for different TRT occupancy ranges and different jet energies are shown in Figures 53 and 54. The simulation describes the experimental data very well.

Figure 55 shows the TRT track extension fraction versus total TRT occupancy for minimum bias events with $40 < \langle\mu\rangle < 70$. In this figure, all tracks down to 0.5 GeV are reconstructed. No dependence on the TRT occupancy is observed and the simulation describes the data well.

Figure 56 shows the number of TRT hits on track as a function of ΔR in jet cores. Some increase of the number of TRT hits on track close to the jet axis is related to an increase of the straw occupancy in the dense track environment close to the jet center.

The most important TRT tracking parameter is the fraction of the hits on the TRT track segment that are precision hits as only precision hits are used in tracking. Such hits are those that provide a drift-radius within about 2.5 measured drift-radius sigmas of the reconstructed track. Figure 57 shows TRT

precision hit fraction versus ΔR in jet cores. A small discrepancy (about 3%) between simulation and data is related to different definitions of the drift-radius sigma caused by differences in the tails of the residual distributions for the data and simulation. The most important result here is that even in the core of the most energetic jets, precision hit fraction is practically the same as that outside of the jet core.

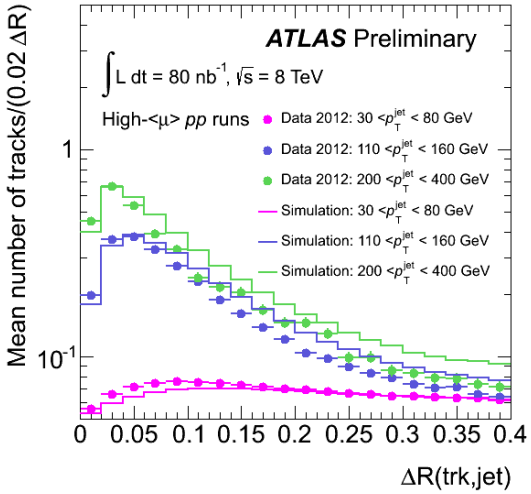

Figure 50: Number of tracks reconstructed in the Inner Detector as a function of ΔR in jet cores for 3 jet p_{T} ranges.

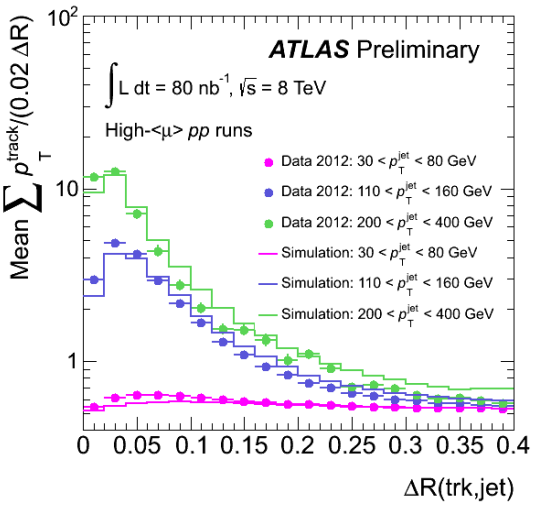

Figure 51: The p_{T} sum reconstructed in jet cores by the Inner Detector as a function of ΔR in the jet cores for 3 jet p_{T} ranges.

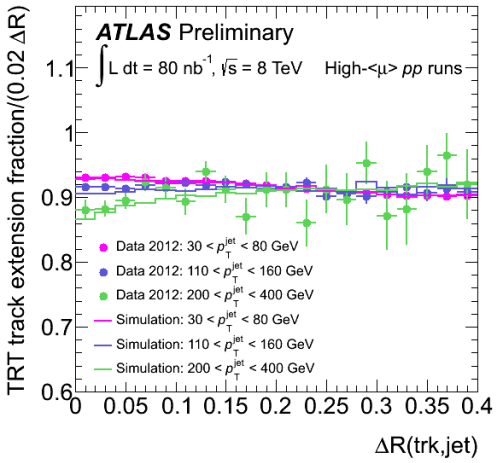

Figure 52: TRT track extension fraction as a function of ΔR in jet cores for 3 jet p_{T} ranges.

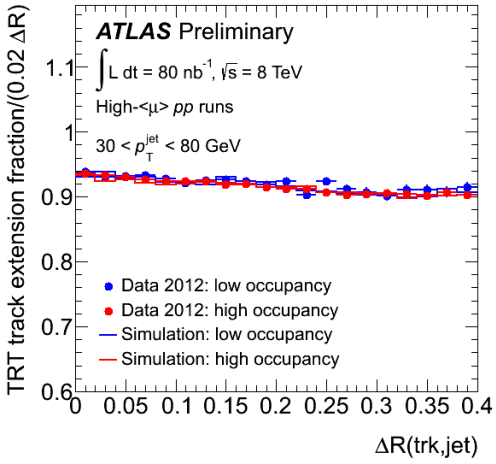

Figure 53: The TRT track extension fraction in jet cores for low (less than 24%) and high (from 34% to 54%) TRT occupancy events as a function of ΔR in the jet cores. The plot is for jets with $30 < p_{\mathrm{T}} < 80$ GeV. Data (points), and simulation (histograms) are shown.

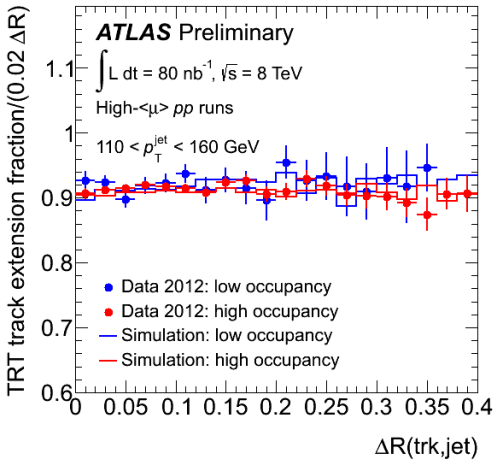

Figure 54: The TRT track extension fraction in jet cores for low (less than 24%) and high (from 34% to 54%) TRT occupancy events as a function of ΔR in the jet cores. The plot is for jets with $110 < p_{\mathrm{T}} < 160$ GeV. Data (points), and simulation (histograms) are shown.

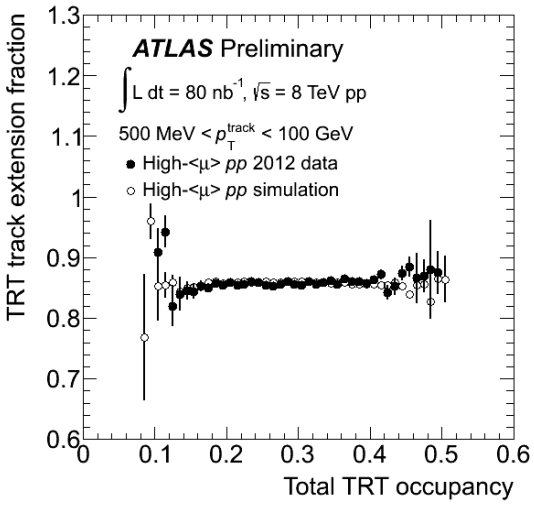

Figure 55: TRT track extension fraction as a function of total TRT occupancy from minimum bias events at $40 < \langle\mu\rangle < 70$.

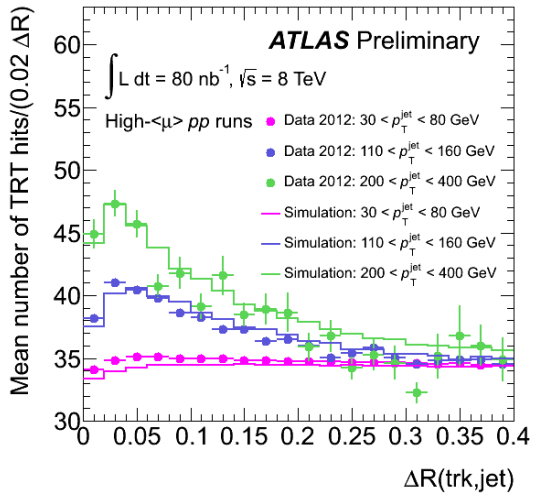

Figure 56: Number of TRT hits on tracks as a function of ΔR in jet cores for 3 jet p_{T} ranges.

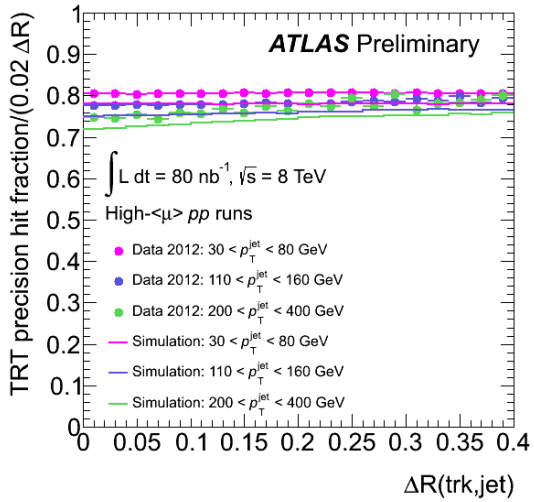

Figure 57: TRT precision hit fraction as a function of ΔR in jet cores for 3 jet p_{T} ranges.

9 Conclusion

A variety of studies about the performance of the ATLAS transition radiation tracker have been shown based on detailed studies using electrons and muons from J/ψ and Z decays and generic tracks inside jets. In all cases the data were compared to simulation, and good agreement is observed at low and high pile-up values.

References

[1] ATLAS Collaboration, *The ATLAS Experiment at the CERN Large Hadron Collider*, JINST **3** (2008) S08003.

[2] ATLAS TRT Collaboration, E. Abat et al., *The ATLAS TRT barrel detector*, JINST **3** (2008) P02014.

[3] ATLAS TRT Collaboration, E. Abat et al., *The ATLAS TRT end-cap detectors*, JINST **3** (2008) P10003.

[4] ATLAS TRT Collaboration, E. Abat et al., *The ATLAS Transition Radiation Tracker (TRT) proportional drift tube: Design and performance*, JINST **3** (2008) P02013.

[5] ATLAS Collaboration, *The ATLAS Simulation Infrastructure*, Eur. Phys. J. **C70** (2010) 823–874.

[6] GEANT4 Collaboration, S. Agostinelli et al., *GEANT4: A simulation toolkit*, Nucl. Inst. Meth. **A506** (2003) 250–303.

[7] ATLAS Collaboration, *Calibration of the ATLAS Transition Radiation Tracker*, ATLAS-CONF-2011-006. http://cdsweb.cern.ch/record/1330712.

[8] ATLAS Collaboration, *Electron performance measurements with the ATLAS detector using the 2010 LHC proton-proton collision data*, Eur. Phys. J. **C72** (2011) 1909.